ACS APPLIED MATERIALS & INTERFACES

Research Article

www.acsami.org

Cocoon-in-Web-Like Superhydrophobic Aerogels from Hydrophilic Polyurea and Use in Environmental Remediation

Nicholas Leventis,* Chakkaravarthy Chidambareswarapattar, Abhishek Bang, and Chariklia Sotiriou-Leventis*

Department of Chemistry, Missouri University of Science and Technology, Rolla, Missouri 65409, United States

Supporting Information

ABSTRACT: Polyurea (PUA) develops H-bonding with water and is inherently hydrophilic. The water contact angle on smooth dense PUA derived from an aliphatic triisocyanate and water was measured at θ = 69.1 ± 0.2°. Nevertheless, texture-related superhydrophobic PUA aerogels (θ' = 150.2°) were prepared from the same monomer in one step with no additives, templates, or surfactants via sol–gel polymerization carried out in polar, weakly H-bonding acetonitrile. Those materials display a unique nanostructure consisting of micrometer-size spheres distributed randomly and trapped in a nanofiber web of the same polymer. Morphostructurally, as well as in terms of their hydrophobic properties, those PUA aerogels are analogous to well-studied electrospun fiber mats incorporating particle-like defects. PUA aerogels have the advantage of easily scalable synthesis and low cost of the raw materials. Despite large contact angles and small contact areas, water droplets (5 μL) stick to the aerogels surface when the substrate is turned upside-down. That so-called Petal effect is traced to H-bonding at the points of contact between the water droplet and the apexes of the roughness of the aerogel surface. Monoliths are flexible and display oleophilicity in inverse order to their hydrophobicity; oil fills all the available open porosity (94% v/v) of cocoon-in-web like aerogels with bulk density ρ_b = 0.073 g cm^{-3}; that capacity for oil absorption is >10:1 w/w and translates into ~6:1 w/v relative to state-of-the-art materials (e.g., graphene-derived aerogels). Oil soaked monoliths float on water and can be harvested off.

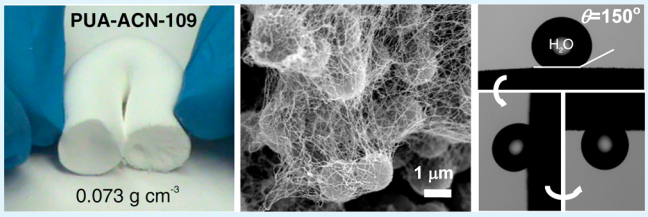

KEYWORDS: *aerogels, polyurea, superhydrophobic, Cassie–Baxter, hydrogen bonding, oil spill cleanup*

1. INTRODUCTION

Hydrophobicity is important for applications in diverse areas ranging from self-cleaning surfaces, prevention of corrosion and biofouling, drag reduction in microfluidic devices, and environmental remediation through oil absorption.[1−4] Hydrophobicity is a surface phenomenon introduced via chemical or textural modification and is quantified with the contact angle, θ, of water droplets on flat surfaces. The upper theoretical limit of θ on smooth close hexagonally packed low-energy CF_3 groups is 119°.[5] However, textured surfaces may display much higher contact angles, often >150°, in which case they are classified as superhydrophobic.

Inspired by Nature, there are two limiting cases for superhydrophobic behavior. In the Lotus effect (from the leaves of the plant[6]), water droplets run off with the slightest tilt of the surface (typically by <5°). The Lotus effect is used by many plants (to stay clean), insects (to stand on water), and animals (to stay dry). In the Petal effect (from the petals of the red rose), a droplet that seemingly barely touches the superhydrophobic surface underneath sticks to it and oftentimes stays in place even when the substrate is turned upside-down.[7] The adhesive force of the Petal effect has been attributed to noncovalent interactions (e.g., van der Waals) and to capillary effects.[8] Both the lotus leaf and the red rose petal are rough, bearing regular patterns of micrometer-sized protrusions whose effect has been replicated and confirmed by molding.[7,9] Artificial superhydrophobic surfaces typically involve multistep processing,[10] e.g., microfabrication of patterns of microbeads, or grass-like nanopillars.[11−13] It is not difficult to contemplate then that, by increasing the aspect ratio of nanopillars, the surface layer evolves into entangled nanofibers (e.g., of carbon, polymer).[14] Owing to the relevance of such surfaces to textiles, a significant body of knowledge has been developed on the basis of electrospinning of nanofiber webs.[15] However, electrospinning, like microfabrication, is also a rather complex process hampered by low rates of production and the high cost of the raw materials. Nevertheless, an important finding from those studies has been that, if electrospun fiber webs include "knots" (normally considered defects), they display higher water contact angles.[16] Introducing nanoparticles (e.g., TiO_2) deliberately has confirmed the role of particles-in-web in terms of increasing hydrophobicity.[17] Those findings render it worthwhile to explore more efficient alternatives for the synthesis of such structures, and a sensible strategy could be based on bulk nanoporous materials.

Received: January 31, 2014
Accepted: April 14, 2014
Published: April 23, 2014

   dx.doi.org/10.1021/am500685k | ACS Appl. Mater. Interfaces 2014, 6, 6872−6882

Scheme 1. Synthesis of Polyurea (PUA) Aerogels

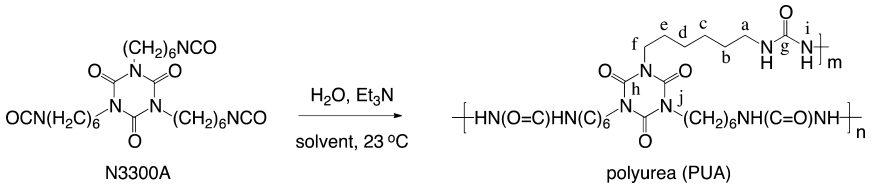

N3300A polyurea (PUA)

In that context, aerogels are inherently nanostructured materials[18] and hence are reasonable platforms for imparting texture related superhydrophobicity. They are prepared easily in bulk form by conversion into a supercritical fluid and venting off the pore-filling solvent of wet-gels. Rendering silica aerogels hydrophobic by introducing surface-CH_3 groups[19] has allowed wet-gels to dry under ambient-pressure and has had an economic impact in terms of large scale production of aerogel pellets for use in thermal insulation.[20] Similarly, polystyrene-cross-linked silica aerogels are hydrophobic ($\theta' = 121°$), and their poly(pentafluorostyrene)-analogues are superhydrophobic ($\theta' = 151°$),[21] which according to the above is attributed to both low surface energy and texture. More recently, cogelation by physical cooling of solutions of syndiotactic polystyrene and high molecular weight poly(ethylene oxide) led to Petal-effect superhydrophobic materials consisting of micrometer-size hydrophilic macropores with submicrometer hydrophobic wells.[22]

In order to simulate the effect of particle-doped electrospun fiber webs, it was deemed reasonable to work with aerogels that already display both nanostructures, fibrous and particulate, depending on the synthetic conditions. Materials of that sort include polyurea (PUA) aerogels synthesized in one step at room temperature in acetone from an inexpensive aliphatic triisocyanate (1,3,5-tris(6-isocyanatohexyl)-1,3,5-triazinane-2,4,6-trione, abbreviated as N3300A) and water using triethylamine (Et_3N) as a catalyst (Scheme 1).[23−25] PUA aerogels have fibrous nanostructures at low monomer concentrations, turning to strings-of-beads and eventually to randomly particulate as density increases.[23] That property is distinctly characteristic of those PUA aerogels, so that density-gradient PUA aerogel monoliths show a morphostructural transition from fibrous to particulate along the direction of increasing density.[24] For the purposes of this study, the specific task was to make both of those extreme forms coexist or to put it differently self-dope PUA fibers with particles of the same material. Such nanostructures were observed when the N3300A/water gelation process was carried out in acetonitrile. The relative amount of fibers to particles varies with the sol-concentration, and at the point where there seems to be a qualitative balance between the two forms (fibers and particles), the material is superhydrophobic, displaying the Petal effect, which is attributed to hydrogen bonding. PUA aerogels of that sort are excellent oil absorbers suitable for environmental remediation.

2. RESULTS AND DISCUSSION

2.1. Synthesis of Polyurea (PUA) Aerogels with Variable Nanomorphology. Figure 1A,B shows the fibrous and particulate nanostructures of a low- and a high-bulk density, ρ_b, PUA aerogel monolith synthesized according to Scheme 1 in acetone. The aerogel density is controlled by the amount of monomer (N3300A) in the sol, for example, for fibrous aerogels with $\rho_b = 0.075$ g cm^{-3}, [N3300A] = 0.109 M

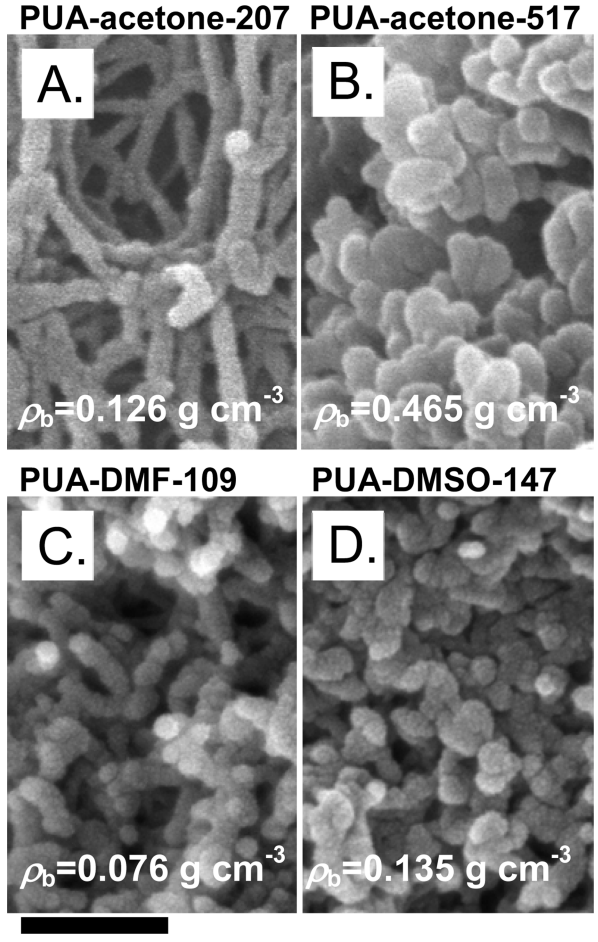

Figure 1. Micromorphology of selected PUA aerogels prepared from the solvents and at the bulk densities (ρ_b) indicated. (Numerical extensions at the sample names indicate the monomer concentration (in mM) in the sol.) Common scale bar for all micrographs at 200 nm.

corresponding to 5.5 g of N3300A in 94 mL of acetone and for particulate PUA aerogels with $\rho_b = 465$ g cm^{-3}, [N3300A] = 0.517 M corresponding to 33 g of N3300A in 94 mL of acetone. Since changing the amount of water (Scheme 1) from stoichiometric (1.5× molar excess) to 2× and 3× the stoichiometric amount or varying the amount of the catalyst did not have an effect on the micromorphology,[23] it was reasoned that the most significant parameter for the fibrous-to-particulate transition was the N3300A/acetone ratio. N3300A is a thick (viscosity $\eta = 2{,}500$ cP) nonpolar (dielectric constant $\varepsilon = 7.8$ at 220 Hz) liquid, which at higher concentrations is expected to modify significantly the properties of acetone sols ($\eta = 0.36$ cP, $\varepsilon = 20.7$). Thus, in the beginning, we sought to emulate and/or partially compensate for the effect of N3300A to the sol by changing the solvent polarity and viscosity. All such materials herewith are denoted as **PUA-solvent-xxx**, whereas **-xxx** stands for the mM concentration of N3300A in

dx.doi.org/10.1021/am500685k | ACS Appl. Mater. Interfaces 2014, 6, 6872−6882

Table 1. Materials Characterization Data for PUA Aerogels Prepared in Three Different Solvents as Indicated

sample[a]	gelation time (min)[b]	linear shrinkage (%)[c,d]	bulk density ρ_b (g cm^{-3})[c]	skeletal density ρ_s (g cm^{-3})[e]	porosity Π (% v/v)	BET surface area σ (m^2 g^{-1})	specific pore volume (cm^3 g^{-1})[f]			pore diameter (nm)[g]	particle radius (nm)[h]	$R(1)$ (nm)[i]	$R(2)$ (nm)[j]
							V_{Total}	$V_{1.7-300\_nm}$	$V_{Total}/V_{1.7-300\_nm}$				
PUA-ACN-109	22 [28.3]	12.4 ± 0.2	0.073 ± 0.002	1.197 ± 0.013	94	25	12.863	0.101	127	19.4 [2058]	100	9.9 ± 0.9	56.8 ± 3.8
PUA-ACN-207	15	11.5 ± 0.1	0.126 ± 0.002	1.177 ± 0.009	89	18	7.0869	0.054	131	16.5 [1575]	142	13.1 ± 0.1	43.1 ± 2.1
PUA-ACN-296	10 [6.35]	10.8 ± 0.1	0.172 ± 0.007	1.201 ± 0.009	86	11	4.981	0.035	142	17.0 [1811]	227	16.6 ± 3.2	43.4 ± 2.9
PUA-ACN-517	7	9.6 ± 0.1	0.347 ± 0.001	1.180 ± 0.004	70	5	2.034	0.013	156	18.7 [1627]	509	10.4 ± 1.9	71.3 ± 4.9
PUA-DMF-109	180 [177.3]	9.4 ± 0.2	0.076 ± 0.002	1.210 ± 0.006	94	307	12.331	1.335	9.24	16.0 [161]	8.1	6.5 ± 0.3	21.3 ± 0.3
PUA-DMF-207	50	39.2 ± 0.3	0.426 ± 0.004	1.270 ± 0.009	66	237	1.560	1.354	1.15	14.9 [26.3]	10.0	12.5 ± 0.0$_3$	*k*
PUA-acetone-109	180 [177.4]	5.7 ± 0.2	0.075 ± 0.003	1.201 ± 0.008	94	187	12.500	0.949	13.2	20.6 [267]	13.4	11.3 ± 0.6	28.4 ± 0.8
PUA-acetone-207	75	9.8 ± 0.1	0.126 ± 0.001	1.265 ± 0.006	90	169	7.146	1.109	6.45	41.6 [169]	14.0	11.9 ± 0.4	27.2 ± 0.8
PUA-acetone-296	30	13.4 ± 0.2	0.172 ± 0.001	1.215 ± 0.002	86	68	4.991	0.465	10.7	40.7 [293]	36.3	19.4 ± 0.1	*k*
PUA-acetone-517	20	19.2 ± 0.1	0.465 ± 0.002	1.200 ± 0.001	61	56	1.317	0.393	3.35	28.3 [94.1]	44.6	47.6 ± 1.3	*k*

[a]Numerical extensions denote the [N3300A] in mM (see text). [b]Phenomenological and [via rheometry] gelation times (data for the latter are shown in Appendix S.1 in the Supporting Information). [c]Average of 5 samples. [d]Linear shrinkage = 100 × [1 − (sample diameter/mold diameter)]. [e]Single sample, average of 50 measurements. [f]$V_{Total} = (1/\rho_b) - (1/\rho_s)$; $V_{1.7-300\_nm}$ is the BJH-desorption cummulative pore volume. [g]By the $4 \times V_{Total}/\sigma$ method whereas V_{Total} was taken using the single-point adsorption method and N_2-sorption data (Figure 4) or, in [brackets], via $V_{Total} = (1/\rho_b) - (1/\rho_s)$. [h]Particle radius from N_2-sorption data = $3/\rho_s\sigma$. [i]Primary particle radii, from SAXS data, first Guinier knee (refer to Appendix S.2 in the Supporting Information). [j]Secondary particle radii, from second Guinier knee. [k]Beyond our accessible low-Q range.

dx.doi.org/10.1021/am500685k | ACS Appl. Mater. Interfaces 2014, 6, 6872−6882

the sol (i.e., [N3300A] = 0.xxx M). When the gelation solvent was switched to more viscous, more polar DMF (η = 0.92 cP, ε = 36.7), it was found that low concentration **PUA-DMF-109** samples consist of short strings-of-beads (Figure 1C). With DMSO (η = 2.24 cP, ε = 46.7), aerogels consisted only of clusters of particles at all concentrations (Figure 1D). Eventually, when the low-viscosity but strongly polar CH_3CN (ACN, η = 0.38 cP, ε = 37.5) was used, we first noticed a drastic decrease in gelation times (<30 min) at all concentrations relative to all other solvents (20 min−3 h, Table 1),[26] but most importantly, ACN-derived aerogels appear as hybrids between those obtained from acetone and from DMSO sols, consisting of spherical moieties trapped in a fiber web. Varying the concentration of N3300A alters the relative ratio of spheres to fibers (Figure 2). As it turns out, **PUA-ACN-109** (ρ_b = 0.073 g cm^{-3}) consist of larger (10 μm in diameter) cocoon-like objects; **PUA-ACN-296** (ρ_b = 0.172 g cm^{-3}) consist of 2 μm diameter isolated spheres entangled in the fiber web; and **PUA-ACN-517** (ρ_b = 0.347 g cm^{-3}) consist mainly of interconnected spheres with a very small amount of fibers. Whenever feasible (that is in the last two cases), at high magnification, fibers seem to emanate and grow out of the smooth surface of the spheres. Although at first approximation **PUA-acetone-xxx** and **PUA-ACN-xxx** share a common evolution from fibrous to particulate as [N3300A] increases, a key difference between the two materials is that particles in **PUA-ACN-xxx** are much larger (micrometer size) than any of those from any other solvent (nanometer size).

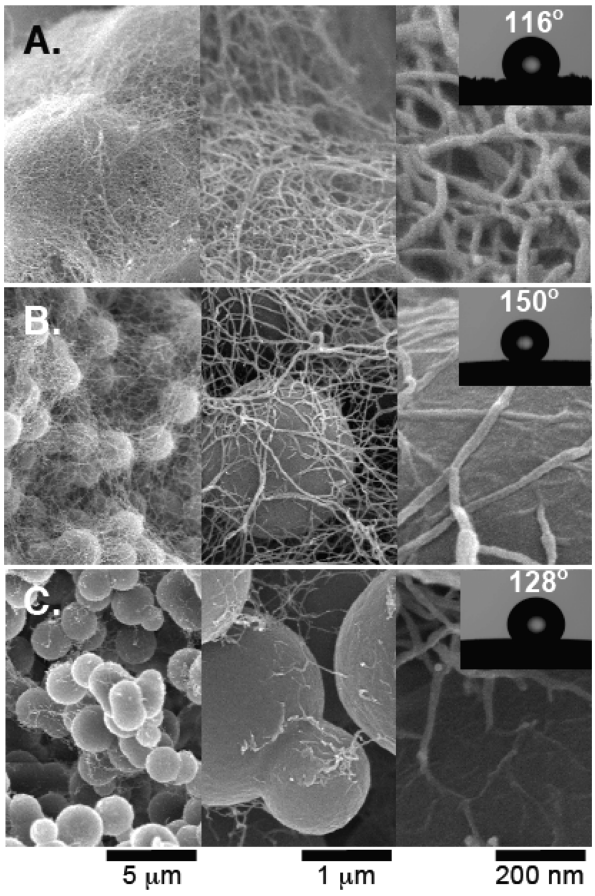

Figure 2. SEM of polyurea aerogels from CH_3CN sols at three different densities and magnifications: (A) **PUA-ACN-109** (ρ_b = 0.073 g cm^{-3}); (B) **PUA-ACN-296** (ρ_b = 0.172 g cm^{-3}); (C) **PUA-ACN-517** (ρ_b = 0.347 g cm^{-3}). Insets: water droplets on flat surfaces and contact angles.

2.2. Chemical and Nanoscopic Characterization. On the basis of solid-state ^{13}C and ^{15}N CPMAS NMR (Figure 3),

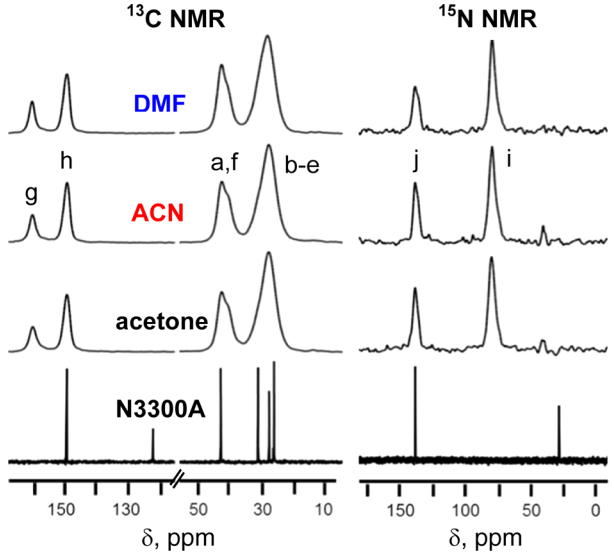

Figure 3. CPMAS solid-state ^{13}C and ^{15}N NMR data of polyurea (PUA) aerogel samples (**xxx** = 109) prepared in the solvent systems as indicated. Bottom: Liquid NMR spectra of the monomer (N3300A) in $CDCl_3$ (^{13}C) and in CD_3NO_2 (^{15}N). All spectra are referenced to glycine-d_5.

the morphological differences reported in section 2.1 above are not associated with drastically different chemical compositions. The −N═C═O ^{13}C and ^{15}N resonances of the N3300A monomer at 122 and 28.5 ppm, respectively, are absent from the spectra of the PUA aerogels. The ^{13}C and ^{15}N resonances of the isocyanurate ring of N3300A at 149 and 138 ppm, respectively, are present at the same positions in the PUA aerogels. The urea carbonyl at 160 ppm retains a constant ratio to the isocyanurate carbonyl in all materials. Similarly, the urea nitrogen at 78 ppm remains constant in all samples. A very small-intensity, almost inconspicuous, resonance at 41 ppm in the ^{15}N NMR spectra of PUA aerogels from acetone or CH_3CN may be due to residual dangling unreacted terminal (surface) amines (i.e., $-(CH_2)_6NH_2$; see Experimental Section).

Despite different nanomorphologies from different solvents, gels from low to medium concentration sols (**xxx** ≤ 296) shrink similarly during processing; consequently bulk densities, ρ_b, and porosities, Π, track each other closely. The pore structures were probed with N_2 sorption porosimetry. The skeletal framework was probed with small-angle X-ray scattering (SAXS) and cross-sectioning with broad beam Ar milling in combination with SEM. Relevant material characterization data are summarized in Table 1.

At low densities, all N_2 adsorption isotherms start rising at relative pressures above P/P_o = 0.9, do not reach saturation, and show narrow hysteresis loops (Figure 4), consistent with mostly macroporous materials, in agreement with SEM. Despite the fibrous morphology of **PUA-acetone-109** (ρ_b = 0.075 g cm^{-3}) and the particulate one of **PUA-DMF-109** (ρ_b = 0.076 g cm^{-3}), their N_2 sorption isotherms track each other closely and the ultimate volumes of N_2 adsorbed are practically equal,

dx.doi.org/10.1021/am500685k | ACS Appl. Mater. Interfaces 2014, 6, 6872−6882

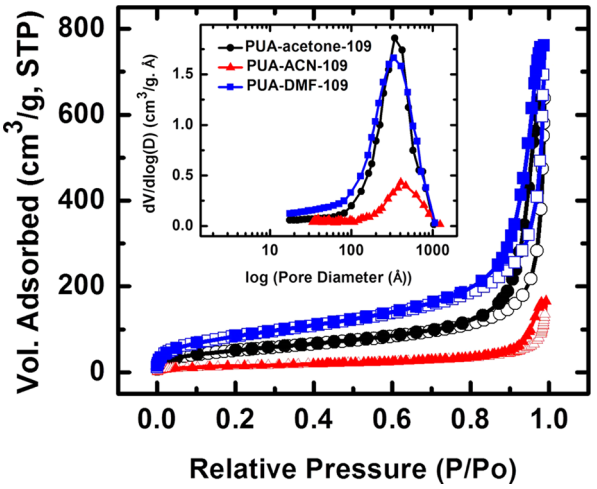

Figure 4. Representative N_2-sorption isotherms (obtained at 77 K) of the three low-density samples (**PUA-solvent-109**) as indicated. Inset: Pore size distributions via the Barrett–Joyner–Halenda (BJH) equation applied to the desorption branches of the corresponding isotherms. (Open symbols: absorption; closed symbols: desorption.) For the summary from the data analysis of all materials, see Table 1.

indicating that the total pore volumes in the 1.7–300 nm range ($V_{1.7-300\_nm}$, Table 1) are similar. Indeed, not only the pore volumes but also the pore size distributions in that range (calculated by the BJH equation applied to the desorption branches of the isotherms; Figure 4, inset) are similar for the two materials (in terms of maxima and widths at half maxima). The proximity of the $V_{1.7-300\_nm}$ values and the similarity of the pore size distributions are a first hint that the fundamental building blocks of the two materials are similar, despite their different SEM nanomorphologies. BET surface areas, σ, differ *only* by a factor of 1.6 (187 $m^2\ g^{-1}$ for **PUA-acetone-109** versus 307 $m^2\ g^{-1}$ for **PUA-DMF-109**). On the other hand, similar density **PUA-ACN-109** aerogels (ρ_b = 0.073 g cm^{-3}) adsorb much less N_2 (the $V_{1.7-300\_nm}$ values are lower by a factor of about 10), and their BET surface area (25 $m^2\ g^{-1}$) is lower than those of samples made in acetone or DMF by a factor of 7.5–12. However, the distribution of pores with sizes in the 1.7–300 nm range is the same in **PUA-ACN-109** as in the other two materials made in acetone and DMF (Figure 4, inset), despite the lower $V_{1.7-300\_nm}$ values. Given that the three materials contain the same amount of matter per unit volume (refer to the similar bulk densities), those data together indicate that (a) all three materials consist, at least partially, of similar elementary building blocks that assemble similarly in the 1.7–300 nm range; however, (b) not all matter in **PUA-ACN-109** is used in that fashion. Because of the much lower amount of N_2 adsorbed, spheres have to be dense objects with no internal structure. Interestingly, as density increases, V_{Total} and $V_{1.7-300\_nm}$ converge for **PUA-acetone-xxx** and **PUA-DMF-xxx** but not so for **PUA-ACN-xxx**. In fact, at higher densities, the value of the $V_{Total}/V_{1.5-300\_nm} \rightarrow 1$ for the first two series of samples, but for **PUA-ACN-xxx** the value of that ratio remains in the 100–150 range (Table 1). Therefore, **PUA-ACN-xxx** always remains macroporous at all densities, suggesting again that most of the polymer remains segregated in a nonporous configuration.

Turning to the skeletal framework, sometimes the origin of X-ray scattering (i.e., from particles or from pores) can be controversial and should be considered together with other experimental observations.[27] Here, on the basis of SEM (Figures 1 and 2) and the high porosity values (Table 1), the dilute phase in PUA aerogels is nanoparticles; therefore, scattering of X-rays arises from 3D distributions of spherical particles,[28] rather than from spherical voids (pores) distributed in another medium.[29] SAXS profiles (Figure S.2 in the Supporting Information) were fitted into two power law regions and two Guinier knees using the Beaucage Unified Model.[30−32] The high-Q power law regions (Q: scattering vector) of all samples (noted as Regions I in Figure S.2 in the Supporting Information) have slopes <−4.0 indicating primary particles with fuzzy (density gradient) interfaces. The high-Q Guinier knees (Regions II in Figure S.2 in the Supporting Information) give the radii of gyration of the primary particles, which in turn are used to calculate the radii of those particles ($R(1)$, included in Table 1). The slopes of the low-Q power law regions (Regions III) give the (mass or surface) fractal dimensions of the secondary particles, and the second Quinier knees (Regions IV) give the radii of gyration and, therefore, the radii of the secondary particles ($R(2)$, Table 1). Primary particles of PUA aerogels with **xxx** < 296 from all solvents are similar in size. (Without affecting this discussion, it is also noted in passing that secondary particles of **PUA-ACN-xxx** samples are surface fractals and a little over double in size than the mass-fractal secondary particles of **PUA-acetone-xxx** and **PUA-DMF-xxx**; refer to Appendix S.2 in the Supporting Information.) Most importantly, in **PUA-acetone-xxx** and **PUA-DMF-xxx**, SAXS radii of primary particles agree *extremely well* with the particle radii calculated from gas sorption and skeletal density data (Table 1); however, by the same token, the SAXS radii of all **PUA-ACN-xxx** are much smaller than those calculated by the latter method. Considering those data together with the similar porosities (Π) and pore size distributions, but much lower $V_{1.7-300\_nm}$ pore volumes and BET surface areas of **PUA-ACN-xxx** relative to those of **PUA-acetone-xxx**, it suggests that only a small fraction of the total material in the **PUA-ACN-xxx** samples has been used for building primary/secondary particle hierarchical structures. Conversely, most of the polymer in **PUA-ACN-xxx** does not contribute to the surface area or to meso/macropore volume that can be probed with N_2-sorption (1.7–300 nm); hence, spheres are dense objects devoid of internal structure. An independent evaluation of this conclusion was obtained by "cutting" through the spheres with an Ar beam followed by SEM (Figure 5), supporting that indeed spheres do not have an internal structure. Furthermore, since the size of those solid dense spheres falls beyond the low Q-range of our SAXS capability, it is concluded that the X-ray scattering profile of **PUA-ACN-xxx** aerogels came from fibers, which therefore, are formed by secondary nanoparticles, which in turn are densely packed surface-fractal assemblies of primary nanoparticles, in agreement with previous conclusions based on small angle neutron scattering of **PUA-acetone-xxx**.[23]

Wet-gel precursors to aerogels are obtained by phase separation under theta-solvent conditions,[33,34] which are achieved either by physical or, as in our case, by chemical cooling. In other words, necessarily, all solvent systems of this study are good solvents for the monomer but not so for the developing polymer. Considering the Hansen solubility parameters (HSP) of our solvents,[35] it is noted that by moving from acetone to DMF to DMSO to CH_3CN the polar contribution (δP) to the HSP increases (from 10.4 to 13.7 to 16.4 to 18, respectively); however, the H-bonding contribution

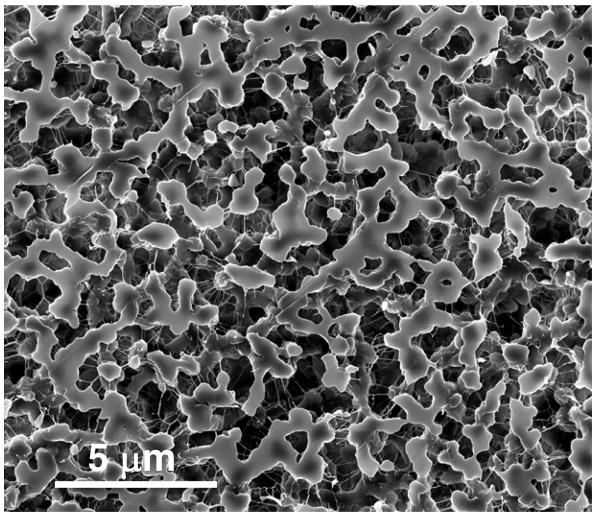

Figure 5. SEM of a **PUA-ACN-296** sample, after cross-sectioning with an Ar beam (see Experimental Section).

(δH) actually moves in the opposite direction, from 7.0 to 11.3 to 10.2, reaching its lowest value with CH_3CN at 6.1. Formation of dense spheres in CH_3CN takes advantage of the weaker hydrogen bonding interactions between the developing polymer and the solvent, causing PUA oligomers to get stabilized by H-bonding to one another and grow into very larger particles. Support for this hypothesis is found in the higher degree of crystallinity in **PUA-ACN-109** samples (67%, by XRD), as opposed to 50% and 40% in the corresponding materials from acetone and DMF, respectively (see Appendix S.3 in the Supporting Information). Closer to the gel point, the remaining monomer concentration is low and a process similar to that taking place in acetone sets in; PUA particles start forming secondary aggregates in solution that, probably for electrostatic/polarizability reasons,[36,37] assemble into fiber-like strings that, for the same reasons, interact and accumulate on reactive protrusions on the surface of spheres, appearing as emanating from the latter (Figure 2). Entanglement of those fibers forms the gel network. In other words, dense spheres are formed first and fibers later.

2.3. Macroscopic Properties. Owing to similar shrinkage, macroscopically **PUA-ACN-xxx** and **PUA-acetone-xxx** aerogels are generally indistinguishable from one another. However, the distinctly different distribution of matter in their interior was expected to have important effects on their bulk properties.

2.3.1. Mechanical Response. Since most of the polymer in **PUA-ACN-xxx** goes to form dense spheres, the weight percent contribution of entangled fibers to the structure is low; hence, **PUA-ACN-xxx** aerogels are much more flexible than the corresponding **PUA-acetone-xxx**. Figure 6 and Movies S.1 and S.2 in the Supporting Information compare the behavior of low-density materials (**xxx** = 109), whereas it can be seen clearly that aerogel cylinders made in acetonitrile can be bent completely (180°), while those made in acetone are far more rigid.

2.3.2. Thermal Conductivity. The dense spheres of **PUA-ACN-xxx** are expected to be thermal shorts that act competitively with the reduced number of interparticle or interfiber contacts and may improve or compromise the thermal resistance of the solid framework. As a result, **PUA-ACN-xxx** could be better or worse thermal insulators than **PUA-acetone-xxx**, which however, could not be decided *a*

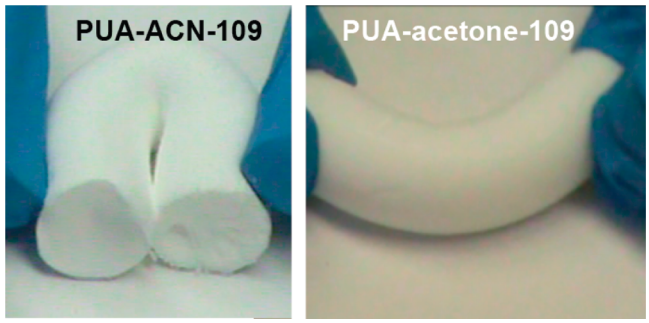

Figure 6. Bending of low-density PUA aerogel monoliths as indicated. Photograph of **PUA-acetone-109** at the break point. See also Movies S.1 and S.2 in the Supporting Information.

priori. Thermal conductivity data for **PUA-ACN-xxx** aerogels at different densities were obtained using the laser flash method (see Appendix S.4 in the Supporting Information). The lowest thermal conductivity was observed with **PUA-ACN-109** (0.032 W m^{-1} K^{-1}), which is at about the lowest limit for this class of materials.[25] Subsequently, the overall thermal conductivity, λ, was separated into a nonconvective (i.e., diffusive) component through the pore-filling gas, λ_g, and a component through the solid framework, λ_s.[38] (Radiative heat transfer was eliminated experimentally.) λ_g was calculated using porosity and pore diameter data (from Table 1) via the Knudsen equation (see Table S.3 in the Supporting Information). It was found (Figure 7) that in the case of **PUA-ACN-xxx** λ_s varies with bulk density

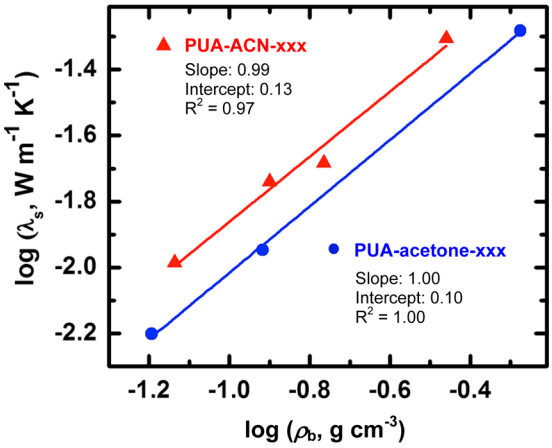

Figure 7. Log–log plot of the solid thermal conductivity, λ_s, versus bulk density of **PUA-ACN-xxx** and **PUA-acetone-xxx** aerogels, as indicated. Data for the latter sample were obtained using the hot-wire method; see ref 25. (Intercepts in W m^{-1} K^{-1}. For the total thermal conductivity, λ, of **PUA-ACN-xxx** aerogels as a function of the bulk density, ρ_b, see Figure S.4A in the Supporting Information.)

according to $\lambda_s = 0.13 \times (\rho_b)^{0.99}$, which is very similar to what we reported recently for **PUA-acetone-xxx**: $\lambda_s = 0.10 \times (\rho_b)^{1.00}$ (using the hot-wire method).[25] In general, exponents of ρ_b equal to 1.0 are akin to foams.[39] In the present case, the equality of the ρ_b-exponents in the two materials underlines the fact that, as far as thermal conduction is concerned, matter fills space macroscopically (i.e., in the length scale of the sample) in the same manner; that is, an increase in density translates into a higher amount of entangled fibers along the heat conduction path. The 30% higher pre-exponential factor for **PUA-ACN-xxx** (0.13 vs 0.10 W m^{-1} s^{-1}) signifies that spheres, being dense

dx.doi.org/10.1021/am500685k | ACS Appl. Mater. Interfaces 2014, 6, 6872–6882

Table 2. Water Contact Angle Data Materials with PUA Aerogels Prepared in Three Different Solvents as Indicated

sample	bulk density ρ_b (g cm^{-3})	porosity Π (% v/v)[a]	contact angle θ' (deg)	C−B fraction f[b]
PUA-ACN-109	0.073 ± 0.002	94	116.2 ± 0.1	0.41
PUA-ACN-207	0.126 ± 0.002	89	133.0 ± 0.1	0.23
PUA-ACN-296	0.172 ± 0.007	86	150.2 ± 0.5	0.10
PUA-ACN-517	0.347 ± 0.001	70	127.6 ± 0.2	0.29
PUA-DMF-109	0.076 ± 0.002	94	104.4 ± 0.1	0.55
PUA-DMF-207	0.426 ± 0.004	66	102.3 ± 0.1	0.58
PUA-acetone-109	0.075 ± 0.003	94	102.4 ± 1.3	0.58
PUA-acetone-207	0.126 ± 0.001	90	97.3 ± 0.1	0.64
PUA-acetone-296	0.172 ± 0.001	86	101.9 ± 0.0	0.59
PUA-acetone-517	0.465 ± 0.002	61	100.1 ± 0.1	0.61

[a]Recited from Table 1 in reference to the relevant discussion. [b]Cassie−Baxter fraction of contact area with the substrate, calculated via eq 2 using θ = 69.1° and the measured θ' for each sample.

Scheme 2. Water Droplet Suspended (Petal Effect) via H-Bonding with Polyurea at the Points of Contact with the Aerogel Surface

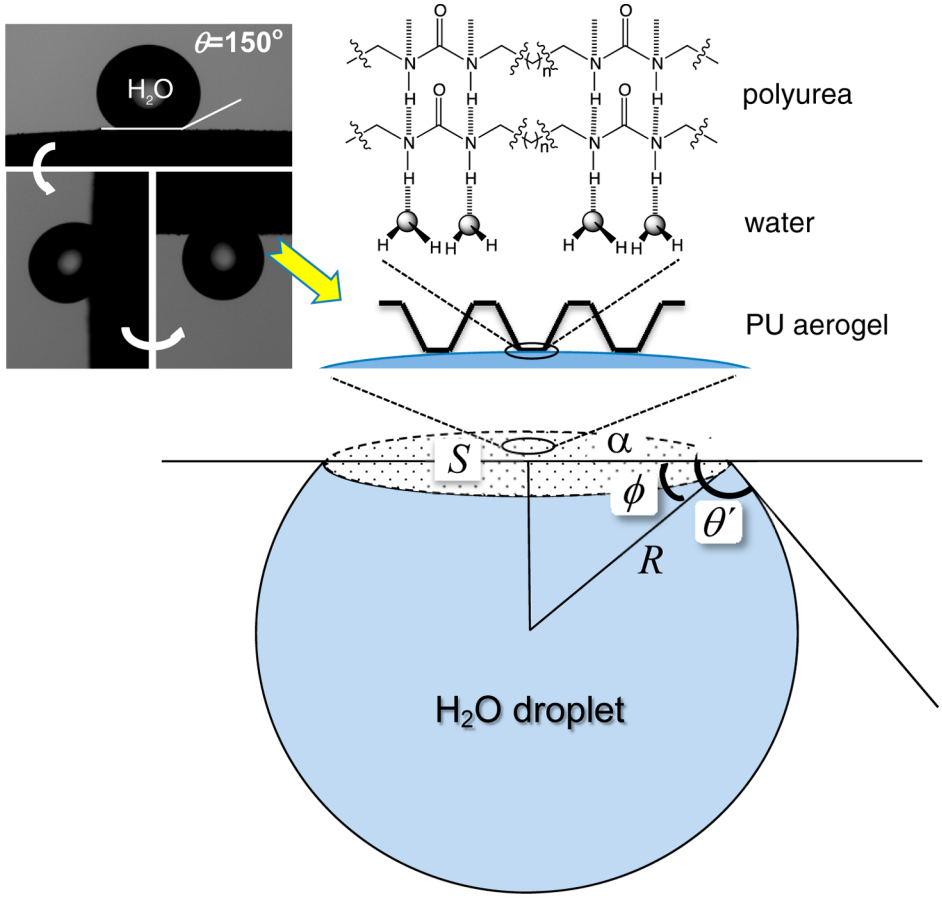

objects, comprise thermal conduits facilitating the overall heat transfer.

2.3.3. Interaction with Water. All PUA aerogels are hydrophobic relative to the smooth polymer, which is hydrophilic (θ = 69.1 ± 0.2°). Contact angles, θ', of 5 μL water droplets on flat internal (fractured) surfaces of **PUA-ACN-xxx** were in the 116°−150° range (Figure 2, insets) but only in the 97°−104° range on either fibrous **PUA-acetone-xxx** or particulate **PUA-DMF-xxx** (Table 2).

Texture-related hydrophobicity is quantified by two models. The Wenzel model considers the surface roughness (r, always >1) and assumes that water enters the crevices between surface features under the droplet. The contact angle on a flat texture surface, θ', is given by eq 1,

$$\cos\theta' = r\cos\theta \quad (1)$$

whereas θ is Young's contact angle on the smooth nontextured material. The Wenzel model predicts superhydrophobicity (i.e., $\cos\theta' \rightarrow -1$) only for materials that are already hydrophobic (i.e., $\theta > 90°$).[40] In the Cassie−Baxter (C−B) model, water does not enter the crevices between surface features; the droplet touches only at the apexes of the roughness (the fakir state).[41] The C−B model is quantified by eq 2,

$$\cos\theta' = f(\cos\theta + 1) - 1 \quad (2)$$

whereas f is the fraction of the actual contact area between droplet and substrate. The C−B model predicts hydrophobicity ($\cos\theta' < 0$) even from *hydrophilic* materials ($\cos\theta > 0$) as long as $f < 1/(\cos\theta + 1)$. This feature is embedded in several reports[42] and is explicitly possible only within the C−B model.

Clearly, all water droplets on PUA aerogels are Cassie−Baxter states, whereas the *only* feature left to differentiate the higher hydrophobicity (higher θ' values) of the ACN-samples is the presence of both fibers and particles. This finding is consistent with the reports from particle-doped electrospun polymeric fiber webs that became the motivation for this work. The largest contact angle ($150.2 \pm 0.5°$) was measured on **PUA-ACN-296** which, qualitatively, shows a more equal balance between the two forms (particles and fibers, Figure 2).

For samples made in acetone or DMF, the C−B contact fractions (f, Table 2, calculated from the experimental θ and θ' values via eq 2) are in the 0.5−0.6 range; for samples made in ACN, f is between 0.1 and 0.4. If f is predicted, as has been suggested,[22] from the sample porosity, Π, via $f = 1 - (\Pi/100)$, then for **PUA-ACN-296** (Π = 86%, Table 2) it is calculated that $\theta' = 144°$. This value is reasonably close to the experimental one (150.2°). However, as noted in the data of Table 2, experimental f values do not vary monotonically with Π, as predicted from $f = 1 - (\Pi/100)$; hence, Π cannot be used as the sole predictor of θ', consistent with the fact that θ' is expected to depend mainly on texture (i.e., pore size and shape) not on the percent of empty volume (porosity).

In spite of the large contact angles, droplets adhere to all PUA surfaces even when substrates are turned upside-down (Petal effect, Scheme 2). Since that effect is independent of texture, it is attributed to hydrogen bonding between water and PUA at the points of contact (Scheme 2).

Indeed, on the basis of the mathematical expression for the volume of a spherical cap $V_{cap} = (1/3)\pi R^3(2 - 3\sin\phi + \sin^3\phi)$ (i.e., the volume of the missing segment from the top of the H_2O droplet shown in Scheme 2)[43] and realizing that the droplet contact angle $\theta' = \phi + (\pi/2)$, the volume of the droplet is given via $V_{droplet} = V_{sphere} - V_{cap}$ by eq 3,

$$V_{droplet} = \frac{\pi\alpha^3}{3\sin^3\theta'}[2 - 3\cos\theta' + \cos^3\theta'] \quad (3)$$

whereas α is the radius of the contact area with the substrate. Setting $V_{droplet}$ = 5 μL and $\theta' = 150.2°$, it is calculated that radius α = 0.053 cm, corresponding to a geometric contact area $S = 8.82 \times 10^{-3}$ cm^2. By considering the Cassie−Baxter contact fraction f = 0.1 (Table 2), the actual contact area is given by $S_{actual} = S \times f = 8.82 \times 10^{-4}$ cm^2. Considering further (a) a ball-park value for monolayer coverage with the N3300A monomer in the range of 10^{-10} to 10^{-12} mol cm^{-2}, (b) three (3) NH···H bonding opportunities with water per repeat monomer unit, and (c) 19 kJ mol^{-1} and 0.2 nm as the average and the typical value for the H-bonding energy and distance,[44] respectively, it is calculated that the water droplet in our particular case interacts with the aerogel substrate with about 5.0×10^{-12} to 5.0×10^{-14} kJ of energy and develops about 0.25−25 N of attractive force with the substrate (via Δenergy = Δforce × Δdistance). That force holds the weight of the droplet (= $V_{droplet} \times \rho_{water} \times$ acceleration of gravity = 4.9×10^{-5} N) when the system is held upside-down (Petal effect) and compensates for the capillary forces in the micrometer-size pores, which over the entire contact area, are estimated via $S \times$ (capillary pressure) = $2S \times (\cos\theta') \times$ (surface tension of water)/(pore radius) to be on the same order of magnitude as the H-bonding forces (around 0.10 N).

Finally, all PUA samples float on water indefinitely. Pulling vacuum does not force water into the pores. Such a C−B to Wenzel transition would take place at a common (for the two models) contact angle, θ', whereas $(f - 1)/(r - f) = \cos\theta$ (by equating eqs 1 and 2). However, all experimental f values together with $\theta = 69.1°$ yield negative roughness (r) values, which is not physically meaningful; hence, a C−B to Wenzel transition cannot take place, as expected from the fact that bulk dense smooth PUA is hydrophilic.

2.4. Oil Absorption and Oil Spill Cleanup with PUA Aerogels. A viable application of porous materials, including aerogels, is in oil spill cleanup.[45] In that regard, hydrophobic PUA aerogel monoliths turn out to be efficient absorbers of nonpolar organic liquids. They remove oil from water fast (Figure 8 and Movie S.3 in the Supporting Information) and

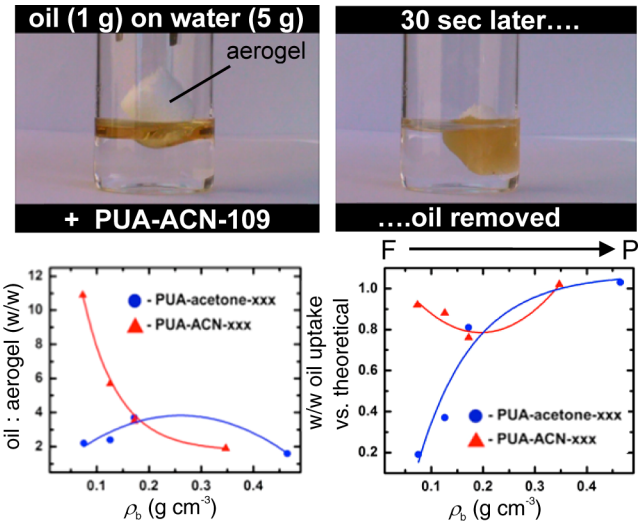

Figure 8. Top: oil removal from water as shown. (Information about the aerogel sample: weight = 0.087 g; volume = 1.19 cm^{-3}; oil/aerogel = 11.5 w/w.) Bottom: Left, gravimetric oil absorption as a function of bulk density. Right: ratio of experimental versus calculated (from porosities, Table 1, and ρ_{oil} = 0.924 g cm^{-3}) oil uptake. Arrow above right frame: transition from fibers (F) to particles (P).

can be harvested off the surface afterward for disposal. Evidently, the oleophilic effect of PUA aerogels is also texture-related: low-ρ_b fibrous/particulate **PUA-ACN-109** absorb about 11× their weight in oil (Figure 8, Bottom (Left)), which is equal to 91% w/w of the possible maximum based on the available porosity (see Figure 8, Bottom (Right)); exclusively fibrous, less hydrophobic **PUA-acetone-109** absorb *only* 2× their weight in oil (25% of their possible maximum). By going to higher-ρ_b, less porous, particulate, **PUA-acetone-517** and **PUA-ACN-517**, the oil uptake is 97% and 100% w/w of the possible maxima, respectively; however, owing to the higher bulk densities (ρ_b) of those monoliths, the oil/aerogel ratio falls to 1.3 and 1.9 w/w, respectively (see Figure 8, Bottom (Left), and Table S.4 in Appendix S.5 in the Supporting Information). The oil capacity of **PUA-ACN-109** (11× w/w) competes favorably with that of polymethyl-silsesquioxane aerogels (6.2 w/w for hexane)[46] and of polystyrene aerogels (5−6× w/w for oil).[47] Recently reported ultralow-density (0.16 mg cm^{-3}) graphene-derived aerogels absorb about 900× w/w of oil;[48] however, underlining a more efficient utilization of the available

dx.doi.org/10.1021/am500685k | ACS Appl. Mater. Interfaces 2014, 6, 6872−6882

space (porosity), **PUA-ACN-109** still absorbs 6× more oil per unit volume (w/v) than those materials and most importantly at a fraction of the cost. It is estimated that, at the current prices of N3300A (about $6/lb), the material cost for removing 1 m^3 of oil from water with **PUA-ACN-109** is about $1,100. In 2014 prices, it would cost about $48.5 M to absorb the 44,000 m^3 of the Exxon-Valdez oil spill. In 1989 dollars, the actual cleanup cost by conventional means was $2B.[49]

3. CONCLUSION

Aerogels are inherently nanostructured materials and hence viable candidates for imparting texture-induced superhydrophobicity. Polyurea is a hydrophilic polymer, which is synthesized here from an aliphatic triisocyanate and water, yielding fibrous or particulate wet-gels and aerogels depending on the gelation solvent and the monomer concentration. All polyurea aerogels from different sols are chemically similar materials, differing significantly only on their degree of crystallinity. From strongly polar, weakly hydrogen-bonding acetonitrile sols, a new nanostructure, unique to our knowledge, has emerged, consisting of dense micrometer-size spherical particles entrapped in nanofiber web. It is suggested that formation of those large particles is driven by H-bonding among developing polyurea oligomers with themselves. Nanostructurally, PUA aerogels synthesized in CH_3CN emulate electrospun polymer mats carrying defects and show similar hydrophobic properties, with contact angles with water droplets that may reach 150°. The great advantage of aerogels of that sort is the time and cost efficient synthesis in bulk quantities. In monolithic form, those materials can be as flexible as a sheet of paper and thermally insulating as other typical aerogels. With an eye into the future, it is known that other polymer aerogels demonstrate fibrous versus particulate nanostructures depending on solvent (e.g., polyimides[50]) or the monomer concentration (e.g., polydicyclopentadiene[51]). It will be worth investigating whether fine adjustment of the solvent properties in those aerogels can yield similar superhydrophobic nanostructures as the ones obtained here with PUA in CH_3CN. Owing to the low cost of the specific PUA materials of this study, it is envisioned that they may be suitable for environmental remediation, whereas harvested oil-soaked aerogels may be disposed directly as fuel.

4. EXPERIMENTAL SECTION

Materials. All reagents and solvents were used as received unless noted otherwise. 1,3,5-Tris(6-isocyanatohexyl)-1,3,5-triazinane-2,4,6-trione was donated generously as a pure compound in bulk form (Desmodur N3300A) by Bayer Corp., U.S.A. A complete spectroscopic characterization of Desmodur N3300A has been given in the Supporting Information of ref 23. Triethylamine, anhydrous acetonitrile (ACN), anhydrous dimethylformamide (DMF), and anhydrous dimethyl sulfoxide (DMSO) as well as HPLC grade acetone, ACN, and DMF were purchased from Aldrich Chemical Co., U.S.A. Anhydrous acetone was purchased from Acros Chemicals, U.S.A.

Preparation of Polyurea (PUA) Aerogels. Polyurea aerogels at different densities were prepared by varying the concentration of Desmodur N3300A. All formulations are summarized in Table 3. In a typical procedure (e.g., for **xxx** = 109), 5.5 g of Desmodur N3300A was dissolved in 94 mL of dry solvent (acetone, ACN, DMF, or DMSO); 3 mol equivalents of water (589 μL) was added, and finally, the sol was obtained by adding 654 μL of triethylamine (0.6% w/w relative to the N3300A plus solvent). Subsequently, the sol was poured into polypropylene molds (Polypropylene Scintillation Vials, General Purpose, 6.5 mL, Sigma-Aldrich Catalogue No. Z376825, 1.27 cm inner diameter), which were sealed with their caps, wrapped with Parafilm, and kept at room temperature for 12 h for gelation and aging. Phenomenological gelation times were recorded by inverting the vials. After aging, gels were removed from the molds, washed with acetone (4× , using 4× the volume of the gel each time), and dried in an autoclave with CO_2 taken out as a supercritical fluid (SCF).

Table 3. Synthesis of PUA-Solvent-xxx Aerogels

sample[a]	N3300A (g [mmol])	solvent (mL)	H_2O (mL)	Et_3N (mL)	[N3300A] (M)
PUA-solvent-109	5.5 [10.9]	94	0.589	0.654	0.109
PUA-solvent-207	11.0 [21.8]	94	1.178	0.700	0.207
PUA-solvent-296	16.5 [32.7]	94	1.767	0.750	0.296
PUA-solvent-517	33.0 [65.5]	94	3.530	0.878	0.517

[a]Solvent: acetone, DMF, CH_3CN.

Methods. *Sol–Gel Transition.* The rheological behavior of selected PUA sols was recorded with a TA Instruments AR 2000ex Rheometer employing an aluminum cone (60 mm diameter, 2° angle) and a Peltier plate using a 1 mm gap, at 20 °C. The instrument was operated in the continuous oscillation mode, and time-sweep experiments were performed with fixed-strain amplitude. The gel-point was determined using a dynamic multiwave method with four superimposed harmonics (1, 2, 4, and 8 rad s^{-1}). The strain of the fundamental oscillation (1 rad s^{-1}) was set at 5%.

SCF Drying. Supercritical fluid (SCF) CO_2 drying was carried out in an autoclave (Speed SFE system, Applied Separations, Allentown, PA).

Physical Characterization. Bulk densities, ρ_b, were calculated from the sample weight and dimensions. Skeletal densities, ρ_s, were determined by helium pycnometry using a Micromeritics AccuPyc II 1340 instrument. Porosities, Π, were determined from ρ_b and ρ_b via $\Pi = (\rho_s - \rho_b)/\rho_s$.

Chemical Characterization. Liquid ^{13}C and ^{15}N NMR spectra of the monomer (N3300A) were obtained with a 400 MHz Varian Unity Inova NMR Instrument in $CDCl_3$ and CD_3NO_2, respectively. The ^{15}N spectrum of N3300A shown in Figure 3 is referenced to glycine-d_5, considering that the ^{15}N resonance of glycine is at −377.0 ppm relative to that of CD_3NO_2. Solid-state ^{13}C NMR spectra were obtained with samples ground into fine powders on a Bruker Avance 300 Spectrometer with a 75.475 MHz carbon frequency using magic angle spinning (at 7 kHz) with broadband proton suppression and the CPMAS-TOSS pulse sequence for spin sideband suppression. Solid-state ^{15}N NMR spectra were obtained on a Bruker Avance 400 Spectrometer with a 40.557 MHz nitrogen frequency using magic angle spinning (at 5 kHz). All other conditions were similar to those used for solid-state ^{13}C NMR. The assignment to dangling unreacted terminal aliphatic $-NH_2$ of the low-intensity ^{15}N resonance at 41 ppm (vs glycine-d_5) in the solid-state spectra of PUA aerogels, made in acetone and CH_3CN, was based on the reported resonance of 1-hexylamine at −357.5 ppm[52] and of 4,4′-methylenedianiline at −323 ppm vs CD_3NO_2.[53] The degree of crystallinity of all PUA aerogels was determined using powder X-ray diffraction (XRD) with a PANalytical X'Pert Pro Multi-Purpose Diffractometer (MPD) with a Cu Kα radiation source (λ = 1.54 Å).

Structural Characterization. N_2 sorption porosimetry was conducted with a Micromeritics ASAP 2020 surface area and porosity analyzer. In preparation for surface area and skeletal density determination, samples were outgassed for 24 h at 40 °C under vacuum. Average pore diameters were determined via the $4 \times V_{Total}/\sigma$ method, where V_{Total} is the total pore volume per gram and σ is the specific surface area determined via the Brunauer–Emmett–Teller (BET) method from the N_2 adsorption data. V_{Total} can be calculated either from the single highest volume of N_2 adsorbed along the adsorption isotherm or via $V_{Total} = (1/\rho_b) - (1/\rho_s)$. Average pore diameter values calculated by both methods are cited in Table 1; when those values converge, the material includes mesoporosity. If the average pore diameter calculated using $V_{Total} = (1/\rho_b) - (1/\rho_s)$ is significantly higher, that is taken as evidence for macroporosity.

The morphology of PUA aerogels was determined with scanning electron microscopy (SEM) using Au-coated samples on a Hitachi S-4700 field emission microscope. The Ilion II Model 697 Broad Beam Argon Milling System (Gatan, Inc. Pleasanton, CA) was used to produce cross sections of the skeletal microspheres for SEM imaging. For this, aerogel monoliths were cut into 2.5 mm thick disks. Half disks (lengthwise) were attached to masks. Samples were milled with an Ar beam (4 kV) at −50 °C for 4 h, until a finely polished area for microscopy and microanalysis was achieved.

The structure of the fundamental building blocks of the materials was probed with small-angle X-ray scattering (SAXS) using 2−3 mm-thick disks, ∼7−10 mm in diameter. SAXS was carried out with a PANalytical X'Pert Pro multipurpose diffractometer (MPD), configured for SAXS using Cu Kα radiation (λ = 1.54 Å) and a 1/32° SAXS slit and a 1/16° antiscatter slit on the incident beam side and 0.1 mm antiscatter slit and Ni 0.125 mm automatic beam attenuator on the diffracted beam side. Samples were placed in circular holders between thin Mylar sheets, and scattering intensities were measured with a point detector in transmission geometry by 2 Theta (2θ) scans ranging from −0.1° up to 5°. All scattering data are reported in arbitrary units as a function of Q ($=4\pi\sin\theta/\lambda$), the momentum transferred during a scattering event. Data analysis was conducted with the Beaucage Unified Model,[30,31] using the *Irena SAS* tool for modeling of small angle scattering,[32] within the commercial *Igor Pro* application (WaveMetrics, Portland, OR).

Thermal Conductivity Characterization. Thermal conductivity, λ, was calculated at 23 °C via $\lambda = R \times c_p \times \rho_b$. Thermal diffusivity, R, was determined with a Netzsch NanoFlash Model LFA 447 flash diffusivity instrument using disk samples ∼1 cm in diameter, 2−3 mm thick. Specific heat capacities, c_p, at 23 °C were measured with powders (5−10 mg) using a TA Instruments Differential Scanning Calorimeter Model Q2000 calibrated against a sapphire standard and run from 0 to 30 °C at 0.5 °C min^{-1} in the modulated T4P mode. Raw c_p data were multiplied by a factor of 1.10 based on measuring the heat capacities of rutile, graphite, and corundum just before running our samples and compared with literature values.

Contact Angle Measurements. Water contact angles were measure using a Rame-Hart Model 250 standard goniometer equipped with a high resolution camera. In the static sessile drop method, a 5 μL droplet of water was placed on the sample surface, the image was capture with the instrument camera, and the contact angle was determined using the DROPimage Advanced v2.4 software. Ten measurements were taken for each specimen, and the results were reported as averages. Aerogel samples were prepared by cutting disks with a knife; surfaces, if necessary, were smoothened using the 3 M Abrasives (320 grit) sand paper (part No. 32541) and were blown over with dry N_2.

Oil Absorption. Oil uptake from aerogels was determined gravimetrically. An excess of used pump oil (Duo Seal Pump oil, density = 0.924 g cm^{-3}) was placed on water; a preweighted aerogel monolith was dropped on top, left to soak for 12 h, removed with a pair of tweezers, strained on paper for 10 min, and then weighed. Results are presented in Appendix S.5 in the Supporting Information.

Dielectric Constant of Desmodur N3300A. The dielectric constant was determined with the aid of a calibration curve from capacitance measurements using an interdigitated electrode array (available from previous work[54]) dipped in several solvents of known capacitance and a METEX M-4650 digital multimeter operated at 220 Hz in the pulse mode.

■ ASSOCIATED CONTENT

Supporting Information

Appendix S.1, rheometry; Appendix S.2, SAXS; Appendix S.3, XRD; Appendix S.4, thermal conductivity; Appendix S.5, oil uptake; Appendix S.6, Movies S.1−S.3 (separate files: am500685k_si_002.avi, am500685k_si_003.avi, and am500685k_si_004.avi, respectively). This material is available free of charge via the Internet at http://pubs.acs.org.

■ AUTHOR INFORMATION

Corresponding Authors

*E-mail: leventis@mst.edu.

*E-mail: cslevent@mst.edu.

Notes

The authors declare no competing financial interest.

■ ACKNOWLEDGMENTS

We thank the Army Research Office for financial support (Award No. W911NF-10-1-0476), the Bayer Corp. U.S.A. for their generous supply of Desmodur N3300A, Catan, Inc. for assistance with broad beam Ar milling, the Materials Research Center of MS&T for support with materials characterization, and Mr. J. Counsil for his assistance with the measurement of the dielectric constant of Desmodur N3300A.

■ REFERENCES

(1) Bocquestt, L.; Lauga, E. A Smooth Future? *Nat. Mater.* **2011**, *10*, 334−337.

(2) Shirtcliffe, N. J.; McHale, G.; Newton, M. I. The Superhydrophobicity of Polymer Surfaces: Recent Developments. *J. Polym. Sci., Part B: Polym. Phys.* **2011**, *49*, 1203−1217.

(3) Callies, M.; Quéré, D. On Water Repellency. *Soft Matter* **2005**, *1*, 55−61.

(4) Zhang, L.; Wu, J.; Wang, Y.; Long, Y.; Zhao, N.; Xu, J. Combination of Bioinspiration: A General Route to Superhydrophobic Particles. *J. Am. Chem. Soc.* **2012**, *134*, 9879−9881.

(5) Ma, M.; Hill, R. M.; Rutledge, G. C. A Review of Recent Results on Superhydrophobic Materials Based on Micro- and Nanofibers. *J. Adhes. Sci. Technol.* **2008**, *22*, 1799−1817.

(6) Barthlott, W.; Neinhuis, C. Purity of the Sacred Lotus or Escape from Contamination in Biological Surfaces. *Planta* **1997**, *202*, 1−8.

(7) Feng, L.; Zhang, Y.; Xi, J.; Zhu, Y.; Wang, N.; Xia, F.; Jiang, L. Petal Effect: A Superhydrophobic State with High Adhesive Force. *Langmuir* **2008**, *24*, 4114−4119.

(8) Dawood, M. K.; Zheng, H.; Liew, T. H.; Leong, K. C.; Foo, Y. L.; Rajagopalan, R.; Khan, S. A.; Choi, W. K. Mimicking Both Petal and Lotus Effects on a Single Silicon Substrate by Tuning the Wettability of Nanostructured Surfaces. *Langmuir* **2011**, *27*, 4126−4133.

(9) Sun, M.; Luo, C.; Xu, L.; Ji, H.; Ouyang, Q.; Yu, D.; Chen, Y. Artificial Lotus Leaf by Nanocasting. *Langmuir* **2005**, *21*, 8978−8981.

(10) See for example: Tuteja, A.; Choi, W.; McKinley, G. H.; Cohen, R. E.; Rubner, M. Design Parameters for Superhydrophobicity and Superoleophobicity. *MRS Bull.* **2008**, *33*, 752−758.

(11) Gu, Z. Z.; Uetsuka, H.; Takahashi, K.; Nakajima, R.; Onishi, H.; Fujishima, A.; Sato, O. Structural Color and the Lotus Effect. *Angew. Chem., Int. Ed.* **2003**, *42*, 894−897.

(12) Öner, D.; McCarthy, T. J. Ultrahydrophobic Surfaces. Effects of Topography Length Scales on Wettability. *Langmuir* **2000**, *16*, 7777−7782.

(13) Bico, J.; Marzolin, C.; Quéré, D. Pearl Drops. *Europhys. Lett.* **1999**, *47*, 220−226.

(14) Li, H.; Wang, X.; Song, Y.; Liu, Y.; Li, Q.; Jiang, L.; Zhu, D. Super-"Amphiphobic" Aligned Carbon Nanotube Films. *Angew. Chem., Int. Ed.* **2001**, *40*, 1743−1746.

(15) Sas, I.; Gorga, R. E.; Joines, J. A.; Thoney, K. A. Literature Review on Superhydrophobic Self-Cleaning Surfaces Produced by Electrospinning. *J. Polym. Sci., Part B: Polym. Phys.* **2012**, *50*, 824−845.

(16) Zhu, Y.; Zhang, J.; Zheng, Y.; Huang, Z.; Feng, L.; Jiang, L. Stable, Superhydrophobic, and Conductive Polyaniline/Polystyrene Films for Corrosive Environments. *Adv. Funct. Mater.* **2006**, *16*, 568−574.

(17) Ogawa, T.; Ding, B.; Sone, Y.; Shiratori, S. Super-Hydrophobic Surfaces of Layer-by-Layer Structured Film-Coated Electrospun Nanofibrous Membranes. *Nanotechnology* **2007**, *18*, 165607−165615.

(18) Pierre, A. C.; Pajonk, G. M. Chemistry of Aerogels and Their Applications. *Chem. Rev.* **2002**, *102*, 4243−4265.

(19) Prakash, S. S.; Brinker, C. J.; Hurd, A. J.; Rao, S. M. Silica Aerogel Films Prepared at Ambient Pressure by Using Surface Derivatization to Induce Reversible Drying Shrinkage. *Nature* **1995**, *374*, 439−443.
(20) Thorne-Banda, H.; Miller, T. Aerogels by Cabot Corporation: Versatile Properties for Many Applications. In *Aerogels Handbook, Advances in Sol-Gel Derived Materials and Technologies*; Aegerter, M. A., Leventis, N., Koebel, M., Eds.; Springer: New York, N.Y., 2011; pp 847−856.
(21) Ilhan, U. F.; Fabrizio, E. F.; McCorkle, L.; Scheiman, D. A.; Dass, A.; Palczer, A.; Meador, M. A. B.; Johnston, J. C.; Leventis, N. Hydrophobic Monolithic Aerogels by Nanocasting Polystyrene in Amine-Modified Silica. *J. Mater. Chem.* **2006**, *16*, 3046−3054.
(22) Wang, X.; Jana, S. C. Tailoring of Morphology and Surface Properties of Syndiotactic Polystyrene Aerogels. *Langmuir* **2013**, *29*, 5589−5598.
(23) Leventis, N.; Sotiriou-Leventis, C.; Chandrasekaran, N.; Mulik, S.; Larimore, Z. J.; Lu, H.; Churu, G.; Mang, J. T. Multifunctional Polyurea Aerogels from Isocyanates and Water. A Structure-Property Case Study. *Chem. Mater.* **2010**, *22*, 6692−6710.
(24) Leventis, N.; Sotiriou-Leventis, C.; Chandrasekaran, N.; Mulik, S.; Chidambareswarapattar, C.; Sadekar, A.; Mohite, D.; Mahadik, S. S.; Larimore, Z.; Lu, H.; Churu, G.; Mang, J. T. Isocyanate-Derived Organic Aerogels: Polyureas, Polyimides, Polyamides. *MRS Proceedings* (2010 MRS Fall Meeting), **2011**, *1306*, 1−12; DOI: 10.1557/opl.2011.90.
(25) Weigold, L.; Mohite, D. P.; Mahadik-Khanolkar, S.; Leventis, N.; Reichenauer, G. Correlation of Microstructure and Thermal Conductivity in Nanoporous Solids: The Case of Polyurea Aerogels Synthesized from an Aliphatic Triisocyanate and Water. *J. Non-Cryst. Solids* **2013**, *368*, 105−111.
(26) It is noted that rheological and phenomenological gelation times (Table 1 and Appendix I in the Supporting Information) match each other closely in all systems; hence, the drastic decrease in gelation times observed in acetonitrile is not associated with, for example, thixotropic states.
(27) Brenner, A. M.; Adkins, B. D.; Spooner, S.; Davis, B. H. Porosity by Small-Angle-X-Ray Scattering (SAXS): Comparison with Results from Mercury Penetration and Nitrogen Adsorption. *J. Non-Cryst. Solids* **1995**, *185*, 74−77.
(28) Dieudonné, Ph.; Delord, P.; Phalippou, J. Small Angle X-ray Scattering of Aerogel Densification. *J. Non-Cryst. Solids* **1998**, *225*, 220−225.
(29) Pujari, P. K.; Sen, D.; Amarendra, G.; Abhaya, S.; Pandey, A. K.; Dutta, D.; Mazumber, S. Study of Pore Structure in Grafted Polymer Membranes Using Slow Positron Beam and Small-Angle X-ray Scattering Techniques. *Nucl. Instrum. Methods Phys. Res., Sect. B* **2007**, *254*, 278−282.
(30) Beaucage, G. Approximations Leading to a Unified Exponential/Power-Law Approach to Small-Angle Scattering. *J. Appl. Crystallogr.* **1995**, *28*, 717−728.
(31) Beaucage, G. Small-Angle Scattering from Polymeric Mass Fractals of Arbitrary Mass-Fractal Dimension. *J. Appl. Crystallogr.* **1996**, *29*, 134−146.
(32) Ilavsky, J.; Jemian, P. R. Irena: Tool Suite for Modeling and Analysis of Small-Angle Scattering. *J. Appl. Crystallogr.* **2009**, *42*, 347−353.
(33) Sheng, Y.-J.; Cheng, K.-L.; Ho, C.-C. Effect of Solvent Quality on the Conformations of a Model Comb Polymer. *J. Chem. Phys.* **2004**, *121*, 1962−1968.
(34) Lambert, S. M.; Song, Y.; Prausnitz, J. M. Theta Conditions in Binary and Multicomponent Polymer Solutions Using a Perturbed Hard-Sphere-Chain Equation of State. *Macromolecules* **1995**, *28*, 4866−4876.
(35) Hansen, C. M. *Hansen Solubility Parameters: A User's Handbook*, 2nd ed.; CRC Press: Boca Raton, FL, 2007.
(36) Zhang, H.; Wang, D. Controlling the Growth of Charged-Nanoparticle Chains through Interparticle Electrostatic Repulsion. *Angew. Chem., Int. Ed.* **2008**, *47*, 3984−3987.
(37) Taden, A.; Landfester, K.; Antonietti, M. Crystallization of Dyes by Directed Aggregation of Colloidal Intermediates: A Model Case. *Langmuir* **2004**, *20*, 957−961.
(38) Parker, W. J.; Jenkins, R. J.; Butler, C. P.; Abbott, G. L. Flash Method of Determining Thermal Diffusivity, Heat Capacity, and Thermal Conductivity. *J. Appl. Phys.* **1961**, *32*, 1679−1684.
(39) Gibson, L. J.; Ashby, M. F. *Cellular Solids-Structure and Properties*, Second Edition; Cambridge University Press: Cambridge, 1999.
(40) Wenzel, R. N. Resistance of Solid Surfaces to Wetting by Water. *Ind. Eng. Chem.* **1936**, *28*, 988−994.
(41) Cassie, A. B. D.; Baxter, S. Wettability of Porous Surfaces. *Trans. Faraday Soc.* **1944**, *40*, 546−551.
(42) See for example: Levkin, P. A.; Svec, F.; Frechet, J. M. Porous Polymer Coatings: A Versatile Approach to Superhydrophobic Surfaces. *Adv. Funct. Mater.* **2009**, *19*, 1993−1998.
(43) http://mathworld.wolfram.com/SphericalCap.html (Accessed 4−5−2014).
(44) Smith, M. B.; March, J. *March's Advanced Organic Chemistry Reactions, Mechanisms, and Structure*; John Wiley & Sons, Inc.: 2001, New York, N.Y.; p 99.
(45) Adebajo, M. O.; Frost, R. L.; Kloprogge, J. T.; Carmody, O.; Kokot, S. Porous Materials for Oil Spill Cleanup: A Review of Synthesis and Absorbing Properties. *J. Porous Mater.* **2003**, *10*, 159−170.
(46) Hayase, G.; Kanamori, K.; Fukuchi, M.; Kaji, H.; Nakanishi, K. Facile Synthesis of Marshmallow-like Macroporous Gels Usable under Harsh Conditions for the Separation of Oil and Water. *Angew. Chem., Int. Ed.* **2013**, *52*, 1986−1989.
(47) Daniel, C.; Alfano, D.; Venditto, V.; Cardea, S.; Reverchon, E.; Larobina, D.; Mensitieri, G.; Guerra, G. Aerogels with a Microporous Crystalline Host Phase. *Adv. Mater.* **2005**, *17*, 1515−1518.
(48) Sun, H.; Xu, Z.; Gao, C. Multifunctional, Ultra-Flyweight, Synergistically Assembled Carbon Aerogels. *Adv. Mater.* **2013**, *25*, 2554−2560.
(49) http://en.wikipedia.org/wiki/Exxon_Valdez_oil_spill (Accessed 1−28−2014).
(50) Meador, M. A. B.; Malow, E. J.; He, Z. J.; McCorkle, L.; Guo, H.; Nguyen, B. N. Synthesis and Properties of Nanoporous Polyimide Aerogels Having a Covalently Bonded Network Structure. *ACS Polym. Prepr.* **2010**, *51*, 265−266.
(51) Bang, A.; Mohite, D.; Sotiriou-Leventis, C.; Leventis, N. Polydicyclopentadiene Aerogels: Nanostructure Control with 1st and 2nd Generation Grubbs Catalysts. *PMSE Prepr.* **2014**, *110*, 000−000.
(52) Sanz, D.; Claramunt, R. M.; Ángeles García, M.; Alkotra, I.; Elguero, J. A ^{13}C and ^{15}N Experimental NMR and Theoretical Study of the Structure of Linear Primary Aliphatic Amines and Ammonium Salts: From C1 to C18. *Tetrahedron* **2011**, *67*, 4633−4639.
(53) Johnston, J. C.; Kuczmarski, M. A. ^{15}N NMR Spectroscopy as a Method for Comparing the Rates of Imidization of Several Diamines. *Polym. Compos.* **2006**, *27*, 723−729.
(54) Dass, A.; Mulik, S.; Sotiriou-Leventis, C.; Leventis, N. Protection of 2-(3-Thienyl)ethanol with 3-Thienylacetic Acid and Hard Cross-Linked Conducting Films by Electropolymerization of the Ester. *Synth. Met.* **2006**, *156*, 966−972.